physchem

MDPI

Article

Structure and Reactivity of $CoFe_2O_4$(001) Surfaces in Contact with a Thin Water Film

Tim Kox, Amir Hossein Omranpoor and Stephane Kenmoe *

Department of Theoretical Chemistry, University of Duisburg-Essen, Universitätsstr. 2, D-45141 Essen, Germany
* Correspondence: stephane.kenmoe@uni-due.de; Tel.: +49-201-183-2497; Fax: +49-201-183-2656

Abstract: $CoFe_2O_4$ is a promising catalytic material for many chemical reactions. We used ab initio molecular dynamic simulations to study the structure and reactivity of the A- and B-terminations of the low-index $CoFe_2O_4$(001) surfaces to water adsorption at room temperature. Upon adsorption, water partly dissociates on both termination with a higher dissociation degree on the A-termination (30% versus 19%). The 2-fold coordinated Fe^{3+}(tet) in the tetrahedral voids and the 5-fold coordinated Fe^{3+}(oct) in the octahedral voids are the main active sites for water dissociation on the A- and B-termination, respectively. Molecular water, hydroxydes, and surface OH resulting from proton transfer to surface oxygens are present on the surfaces. Both water-free surface terminations undergo reconstruction. The outermost Fe^{3+}(tet) on the A-termination and B-termination move towards the nearby unoccupied octahedral voids. In the presence of a thin film of 32 water molecules, the reconstructions are partially and completely lifted on the A- and B-termination, respectively.

Keywords: molecular dynamics; $CoFe_2O_4$; inverse spinel; water dissociation; surface reconstructions; proton transfer

check for updates

Citation: Kox, T.; Omranpoor, A.H.; Kenmoe, S. Structure and Reactivity of $CoFe_2O_4$(001) Surfaces in Contact with a Thin Water Film. *Physchem* **2022**, *2*, 321–333. https://doi.org/10.3390/physchem2040023

Academic Editor: Andrei Kovalevsky

Received: 1 August 2022
Accepted: 10 October 2022
Published: 17 October 2022

1. Introduction

Spinel-type transition metal oxides (TMO) are increasingly being used as catalysts for the production of chemicals at the industrial level via heterogeneous catalysis. This stems from their interesting electronic, magnetic, optical, electrical, thermal and redox properties [1]. Among these, cobalt ferrite ($CoFe_2O_4$) was found to be a promising catalytic material for many chemical reactions due to its unique structural and chemical stability [2–4]. These include the oxygen evolution reaction (OER) [5–8], CO oxidation [8–12], 2-propanol oxidation [13,14], alkene oxidation [15], methane combustion [16] and the oxidation of many other organic compounds [17].

$CoFe_2O_4$ nanoparticles naturally grow as octahedrons, exposing only the low index (111) facet. This stems from the surface energy of this facet (0.208 $J \cdot m^{-2}$) which is one order of magnitude lower than the two other low index (001) and (101) facets (1.486 $J \cdot m^{-2}$ and 1.916 $J \cdot m^{-2}$, respectively) as calculated by Zheng et al. [18]. Based on these surfaces energies, they computed the equilibrium shape of $CoFe_2O_4$ using a Wulff construction. Their calculations showed octahedral grains exposing 8 (111) facets only, in agreement with the experimentally observed scanning electron microscopy (SEM) images [19].

However, in operando, it may happen that less stable facets show a better catalytic performance for particular chemical reactions. Control parameters such as the solvent may act as selective surfactants and promote the growth of a particular surface termination [20]. In this respect, the performance the (111) facet for OER was recently questioned by Hajiyani et al. as a considerable disagreement between the calculated and experimental overpotentials was observed [5,6,21]. Using DFT calculations, they investigated the catalytic performance of pure and chemically modified $CoFe_2O_4$(001) surfaces for OER and found that this less stable facet shows a lower overpotential [21].

Additionally, several synthesis routes have been developed in recent years to tune the size, shape and composition of $CoFe_2O_4$ nanoparticles and promote a selective exposure of

catalytically relevant facets. Depending on the interplay between the synthesis parameters such as temperature, reaction time and solvent, nanoparticles with various shapes can be synthesized [22]. For example, Kim et al. recently proposed a recipe that enables the growth of highly crystalline nanohexagons exposing not only the (111) facets but also the (001) facets in considerable proportions [23]. Apart from temperature and reaction time, the ratio of surfactant to solvent was found to be a decisive parameter in their study. Hence, for a rational design and improvement of the properties of $CoFe_2O_4$ nanoparticles, the role of the solvent should be elucidated.

Recently, a primordial step towards understanding the effect of aqueous solvation on the properties of $CoFe_2O_4$ nanoparticles was performed by Rushiti et al. [24]. They used static DFT calculations to investigate the structure and reactivity of clean and O-defected $CoFe_2O_4$(001) surface towards water in the single molecule regime. Water was found to adsorb a mainly molecularly form on Co and Fe metal sites of defect-free surfaces, whereas it always dissociates at oxygen vacancies, thereby lifting the reconstructions introduced by the defects.

However, for processes in operando, the dynamical character of the disordered liquid water phase and the thermal contributions to its structure and reactivity have to be taken into account. In this work, we used ab initio molecular dynamic simulations to shed some light on the structural response and reactivity of $CoFe_2O_4$(001) surfaces to water adsorption at room temperature. We investigated the nature of the adsorption sites and the chemical state of water in the contact layers. We consider both the so-called A- and B-terminations of $CoFe_2O_4$(001) and a water film of approximately 2 Å to 3 Å and consisting of 32 water molecules. As shown in previous studies, this thickness of interfacial water describes reasonably well the interface between water and many oxides [20,25–28].

2. Computational Details

Cobalt ferrite ($CoFe_2O_4$) crystallizes in a face cubic centered inverse spinel [2], with an inversion degree that depends on the synthesis conditions. In this work, we consider a full inverse spinel structure, where 1/4 of the octahedral voids are co-occupied by cobalt Co^{2+}(oct) and Fe^{3+}(oct), while the tetrahedral voids are only occupied by Fe^{3+}(tet). We alternate the occupation of the octahedral voids with Co^{2+} and Fe^{3+} with every layer in the x direction (surface in-plane), (see Figure 1).

Cutting in the (001) direction leads to two different surface terminations known as A- and B-terminations (see Figure 2). The topmost layer (L0) of the A-termination shows only 2-fold coordinated Fe^{3+}(tet) ions occupying the tetrahedral voids, while the topmost layer (L1) of the B-termination is mixed, consisting of 5-fold coordinated Co^{2+}(oct) and Fe^{3+}(oct) ions which sit in the octahedral voids and surface oxygens.

To model the interaction of the surfaces with the water film, non-stoichiometric slabs consisting of 11 and 13 atomic layers covered with a water film of 32 molecules and followed by a vacuum region of approximately 20 Å thickness were used for A- and B-termination, respectively. In each case, five (A-termination) and six (B-termination) atomic layers in the bottom part of the slabs were frozen at their bulk positions and the upper part of the slab allowed to relax together with the water molecules. A supercell with (2×2) periodicity in the lateral direction (x and y) and corresponding dimensions of 16.784 Å $\times$ 16.784 Å $\times$ 40.0 Å was used. A dipole correction was applied in the surface's out of plane direction to cancel the electric field gradient in the vacuum, arising from the asymmetry of the slabs due to the frozen atoms in the bottom part and the one-sided water adsorption.

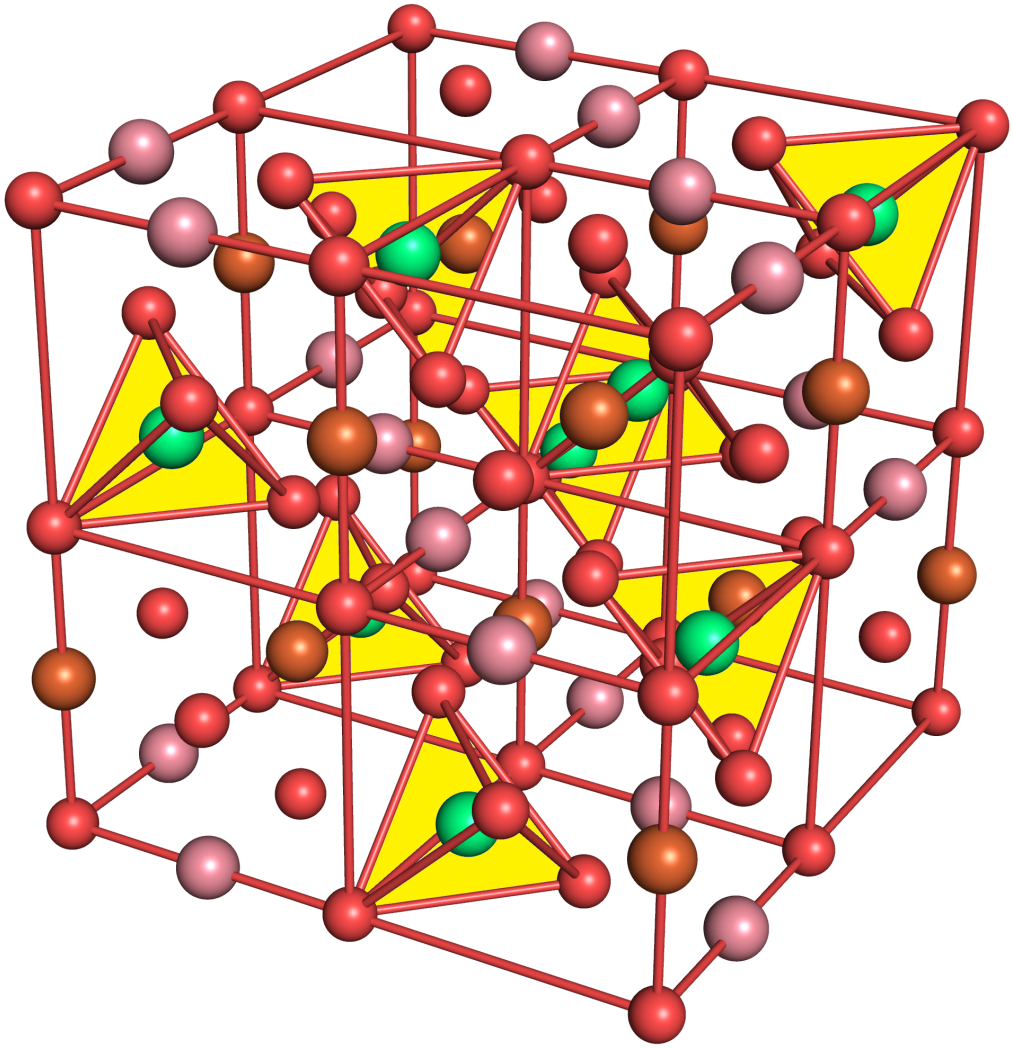

Figure 1. $CoFe_2O_4$ bulk structure. Fe^{3+}(tet) ions in tetrahedral voids (yellow) are shown in green, Fe^{3+}(oct) and Co^{2+}(oct) ions in octahedral voids in brown and purple and oxygen atoms in red.

The CP2K/Quickstep package [29] was used to perform Born-Oppenheimer molecular dynamics (MD) simulations. The electronic interactions were treated with the PBE exchange-correlation functional [30] together with a dispersion correction of the Grimme D3 type [31]. Hubbard correction [32] terms of $U = 2.0$ eV [26,33–35] for Co and $U = 3.3$ eV [36] for Fe were added for a correct description of their 3*d* states. The core electrons were treated with Goedecker–Teter–Hutter (GTH) pseudopotentials, while the 3s, 3p, 3d, and 4s, electrons of Co and Fe atoms and the 2s and 2p electrons of the O atoms were considered valence electrons. The basis sets consisted of a mixture of double-ζ quality local basis functions with one set of polarization functions (DZVP) and plane waves with a cutoff of 500 Ry.

The Born–Oppenheimer molecular dynamics trajectories were propagated with a time step of 0.5 fs during a total simulation time of 20 ps. To achieve NVT conditions, a Nosé–Hoover thermostat with a time constant of 1 ps and a target temperature of 300 K was used.

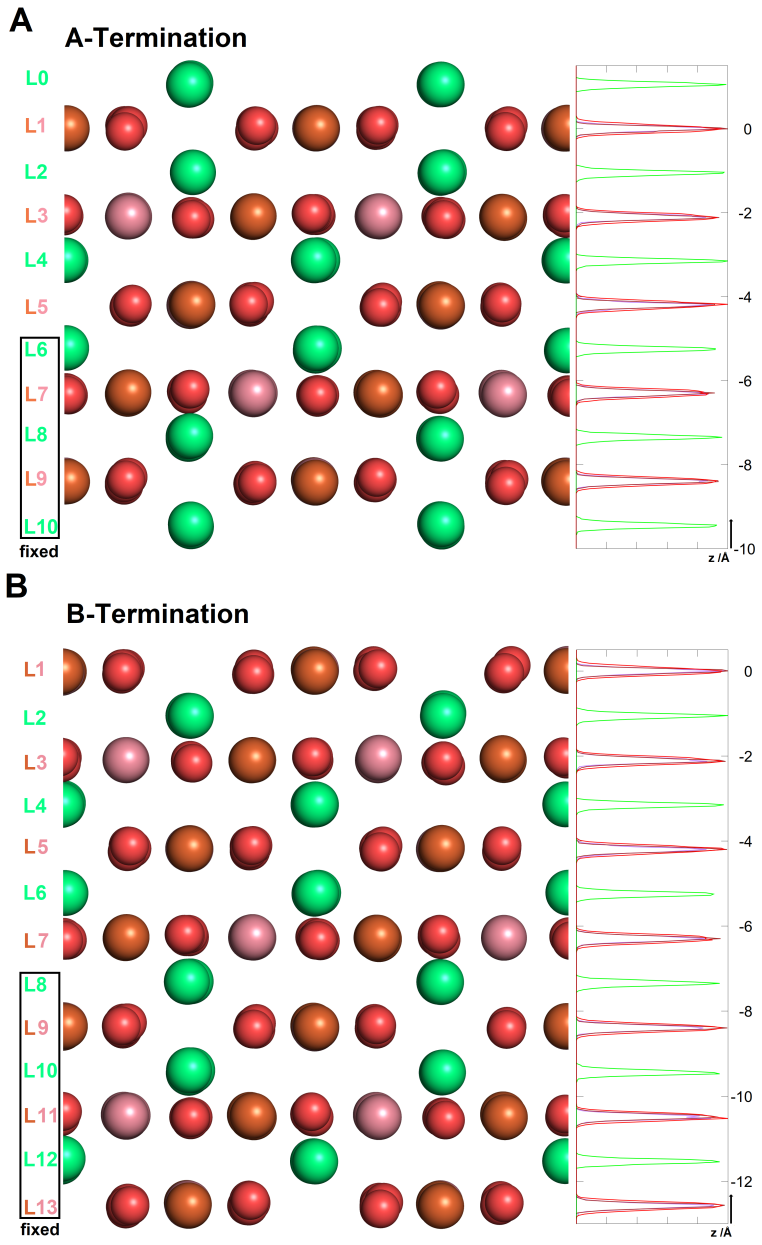

Figure 2. A-(top) and B-(bottom) terminations of the $CoFe_2O_4(001)$ surface. Fe^{3+}(tet) ions in tetrahedral voids are shown in green, Fe^{3+}(oct) and Co^{2+}(oct) ions in octahedral voids are shown in brown and purple and oxygen atoms are shown in red. On the left, various layers are defined, and atom density profiles along the *z* axis are shown on the right. Layers L6–L10 and L8–L13 were kept rigid for A- and B-terminations, respectively.

3. Results and Discussion

3.1. The Structure of Interfacial Water

The A- and B-terminations of the $CoFe_2O_4(001)$ surface show open surfaces where water can bind on several potential adsorption sites. These are the 2-fold coordinated Fe^{3+}(tet), the 5-fold coordinated Co^{2+}(oct) and Fe^{3+}(oct). On both terminations, one differentiates between surface oxygens O1 in the topmost layer (L1) that is bound to one Fe^{3+}(tet) in the nearest subsurface layer L2 and that which is not (O2). To investigate the adsorption mode of water at the interface, we calculated the characteristic radial distribution functions between the surface cations and anions and water adsorbates on the A- and B-terminations.

3.1.1. A-Termination

Thirty-two potential adsorption sites are present on this surface: the cobalt and iron ions in the octahedral voids (16) and the 8 iron ions in the tetrahedral voids on which up to two molecules can adsorb. As seen from snapshots of equilibrium trajectories (Figure 3A), both water molecules, water OH groups and surface OH arising from proton transfer are present in the contact layer.

Figure 4 (left) shows the bond length distances between surface cations and water oxygens. While molecular water is present at all adsorption sites as exteriorized by the peaks centered at 2.15 Å, 2.25 Å and 2.35 Å for Fe^{3+}(tet), Co^{2+}(oct) and Fe^{3+}(oct), respectively. It is seen that hydroxides bind preferentially on Co^{2+}(oct) and Fe^{3+}(tet) with a stronger signature on the latter sites, as shown by the intensity of the peaks centered at 1.9 Å and 1.95 Å, respectively. Hydroxides are barely present on the Fe^{3+}(oct) sites, as seen from the broad peak of very low amplitude centered at 2.20 Å.

Our investigations reveal that approximately 21 (21.4) adsorbates are present in the contact layer with the surface, 7.1 hydroxides and 14.3 water molecules. The distribution of adsorbates on the adsorption sites reads: 8.8 molecules on Fe^{3+}(tet), 7.5 and 5.1 on Fe^{3+}(oct) and Co^{2+}(oct), respectively. Furthermore, 5.4 out of 7.1 hydroxides bind on Fe^{3+}(tet), confirming the stronger preference of water to dissociate on these sites, as mentioned above.

Figure 4 (right) shows the radial distribution function of the different surface oxygen types to the water hydrogens. One can see a signature of H-bonding between the surface O1 and water hydrogens as highlighted by the peak at 1.8 Å. The characteristic peaks at 1 Å show a more significant presence of hydrogens bound to the O1 surface oxygens compared to O2 surface oxygens. This stems from the fact that proton transfer on the latter occurs only upon the reconstruction of some of the nearby Fe^{3+}(tet) that move away from the tetrahedral voids, annihilating the steric effects that prohibit proton transfer to surface O2 oxygens.

3.1.2. B-Termination

In the case of the B-terminated surface, 16 potential adsorption sites are present, which are the 8 Co^{2+}(oct) and 8 Fe^{3+}(oct). On each site, only one water or hydroxide molecule can adsorb. Unlike on the A-termination, water sits on all adsorption sites. As seen from Figure 3B, water adsorbs via a partly dissociative mode, with a lower dissociation degree compared to the A-termination. Figure 5 (left) shows the radial distribution function between the surface cations and water oxygens. Hydroxide molecules almost exclusively bind on Fe^{3+}(oct) sites. This is supported by the peak centered at 1.95 Å, the characteristic signature of OH groups which is quenched for Co^{2+}(oct) and which interact exclusively with molecular water.

The integration of the number density shows that 3.1 water molecules out of the 16 present in the contact layer dissociate via proton transfer to the surface. This exclusively occurs on surface oxygens O2, as shown in Figure 5 (right), in which the characteristic peak at 1.05 Å, which is the signature of surface OH originating from the proton transfer to the surface, is missing for surface oxygens O1. Furthermore, surface oxygens O2 is predominant in the hydrogen bonding to the surface, as can be seen from the peak centered at 1.75 Å which also exteriorizes a strong H-bonding character.

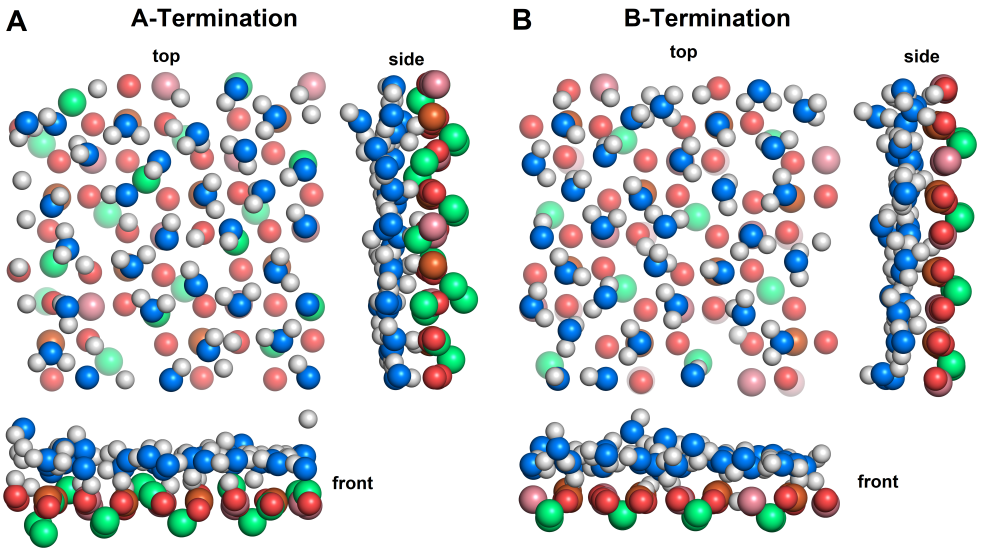

Figure 3. Snapshots of final configurations of each simulation. Fe^{3+}(tet) : green, Fe^{3+}(oct): brown, Co^{2+}(oct) : purple, slab oxygens: red, water/hydroxide oxygen: blue, hydrogen: white. Greyed-out atoms are located in lower layers.

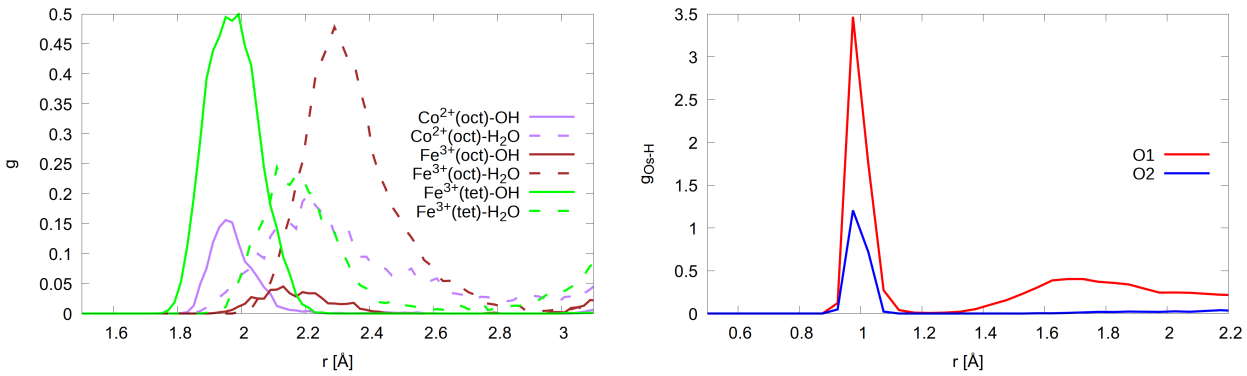

Figure 4. Radial distribution function of the adsorptions sites to the oxygen of water and hydroxide molecules (**left**) and the radial distribution function of the two lattice oxygen types (O1, O2) to hydrogen (**right**), A-termination.

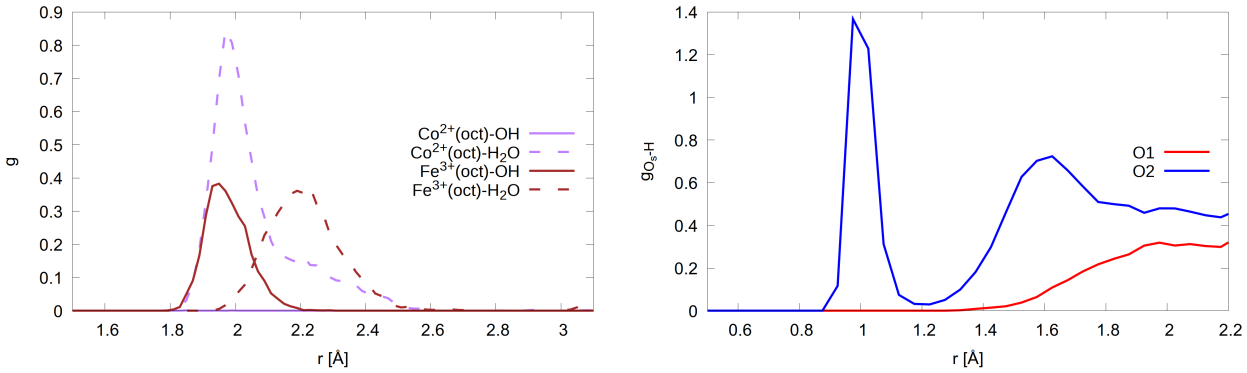

Figure 5. Radial distribution function of the adsorptions sites to the oxygen of water and hydroxide molecules (**left**) and the radial distribution function of the two lattice oxygen types (O1, O2) to hydrogen (**right**), B-termination.

3.2. Surface Relaxations and Reconstructions

To study the structural behavior of the A- and B- surfaces' terminations upon water adsorption, for each surface termination, we performed molecular dynamics runs at room

temperature for simulations times of 20 ps for the water-free and water-covered surfaces, respectively. Afterwards, we computed and analyzed the characteristic density profiles and radial distribution functions (RDFs) to investigate the changes in the geometrical features before and after the simulations taking the clean surfaces as references.

3.2.1. A-Termination

After the relaxation of the water-free surface, the tetrahedral voids containing the Fe^{3+}(tet) are widened (6 out of 8 Fe^{3+}(tet) in the topmost layer L0) as these ions move towards the nearby unoccupied octahedral voids in L1 (Figure 6 top left, bottom left). This is supported by Figure 7 (top left) that shows the distances between Fe^{3+}(tet) in L0 and L2 and the surface O of the tetrahedral voids located in the adjacent layers L1 and L3, respectively. For the clean surface, Fe^{3+}(tet) in L0 are displaced by approximately 0.05 Å from their bulk positions, as shown by the peak at 1.95 Å. Additionally, the broader peak's shoulder of lower amplitude at 2.2 Åarises as the Fe^{3+}(tet) moves closer to the surface oxygens located in the unoccupied octahedral voids in L1. These Fe^{3+}(tet) in L0 weakly interact with the lattice oxygens located in the unoccupied octahedral void in L3, as illustrated by the peak 2.8 Å. The presence of water slightly attenuates these relaxation features (Figure 6 top right, bottom right) as illustrated by the lower amplitude of the RDFs (blue lines in Figure 7, top left). The Fe^{3+}(tet) in the inner layer L2 also shows this tendency to move towards the octahedral voids, but the effect is not as pronounced as in the topmost layer L0, as shown by the faster convergence of the radial distribution functions towards bulk values under dry and humid conditions (dashed lines in Figure 7, top left). Only 2 out of 8 Fe^{3+}(tet) reconstruct in L2.

The reconstruction of Fe^{3+}(tet), as they move towards the nearby unoccupied octahedral voids, yields an increment in the coordination number in the outermost surface layers. The calculated coordination numbers for the clean surface read 4.87, 4.50 and 4.01 for Fe^{3+}(tet) in layers L0, L2 and L4, respectively. As a consequence of water adsorption, the coordination number of Fe^{3+}(tet) in the contact layer with water increases to 5.45, while the coordination environment of Fe^{3+}(tet) in the inner layers remains almost unchanged with coordination numbers of 4.45 and 4.01 for Fe^{3+}(tet) in layers L2 and L4. The out-of-plane distribution of Fe^{3+}(tet) displayed in Figure 7 (top right) shows that the outermost Fe^{3+}(tet) undergoes an inwards relaxation, moving closer to L1 as illustrated by the shift by approximately 0.5 Å to lower values from the bulk positions. The peak intensity is attenuated by water adsorption and spreads until bulk positions as the coordination environment of Fe^{3+}(tet) ions changes as mentioned above.

As a consequence of the clean surface reconstruction, octahedral voids containing the Co^{2+}(oct) shrink (Figure 6 top left, bottom left) as supported by Co^{2+}(oct)–Os distances that shift to a lower value by approximately 0.5 Å compared to bulk (Figure 7, centre left). Fe^{3+}(oct) undergo relaxations of small amplitude, as can be seen from (Figure 7, bottom left). Upon water adsorption, the voids are enlarged as illustrated by larger Fe^{3+}(oct)–Os distances. Co^{2+}(oct) and Fe^{3+}(oct) undergo inwards and outwards out-of-plane relaxation of very weak amplitude, as shown in Figure 7 (centre right, bottom right), respectively. This observation also holds in the presence of water as the density profiles are very similar. Water adsorption yields a bulk-like coordination environment (coordination numbers of 5.86 and 5.6 for Fe^{3+}(oct) and Co^{2+}(oct), respectively, vs. 6 for the bulk coordination number).

3.2.2. B-Termination

Fe^{3+}(tet), located in L2, reconstructs on the clean surface (3 out of 8 Fe^{3+}(tet)) by moving into unoccupied octahedral voids in L1 (Figure 8 top left, bottom left), as highlighted by the tail in the RDF (Figure 9, top left) and the presence of the peak at –0.1 Å in their density profiles which express an outwards relaxation by approximately 0.9 Å (Figure 9, top right). This increases the coordination number of outermost Fe^{3+}(tet) to 4.38. Their counterparts in the inner layers L4 and L6 do not reconstruct and their coordination numbers barely deviate from bulk values (4.03 and 4.07, respectively). Upon water adsorption, the reconstruction

in L2 is lifted as the presence of water quenches the aforementioned geometric features. As a consequence, the Fe^{3+}(tet) in L2 recover their bulk environment with a coordination number of 4.02.

Like on the A-termination, a consequence of the Fe^{3+}(tet) reconstruction is the shrinking of the octahedral voids containing the Co^{2+}(oct) that can be observed in the L1 layer (Figure 8 top left, bottom left). The shortening of the Co^{2+}(oct)–Os distances, as shown in Figure 9 (centre left) supports this observation. This holds under dry and humid conditions (Figure 8 top right, bottom right). Figure 9 (centre right) shows that the Co^{2+}(oct) undergoes almost no out-of-plane relaxation. This is a consequence of the weaker interaction of Co^{2+}(oct) with water, as shown in Figure 5 (left) and discussed above. Water enlarges the octahedral voids containing the Fe^{3+}(oct) as it can be seen from the broadening of the RDF of the outermost Fe^{3+}(oct) in Figure 9 (bottom left) and their outwards out-of-plane relaxation in Figure 9 (bottom right). This stems from their stronger interaction with water hydroxide. Furthermore, like the Fe^{3+}(tet), upon water adsorption, the 5-fold coordinated Fe^{3+}(oct) and Co^{2+}(oct) recover their bulk coordination number of 6.

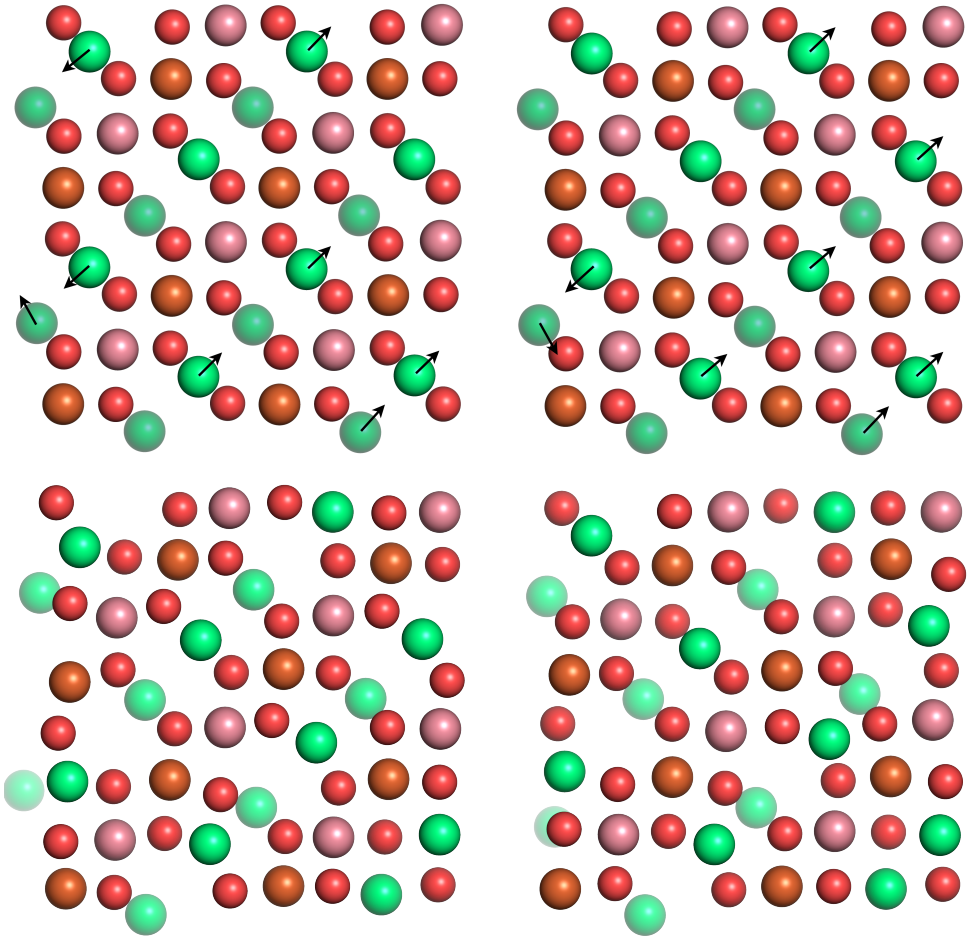

Figure 6. Top views of the initial (top row) and final (after 20 ps; bottom row) surface structures for A-terminated water-free (**left**) and water covered (**right**) $CoFe_2O_4$(001) surfaces, with atom coloring Fe^{3+}(oct): brown, Fe^{3+}(tet): green, Co^{2+}: purple, O: red as in Figure 2. Fe^{3+}(tet) ions below the top surface layers are partially greyed out. The arrows indicate the reconstruction of the Fe^{3+}(tet).

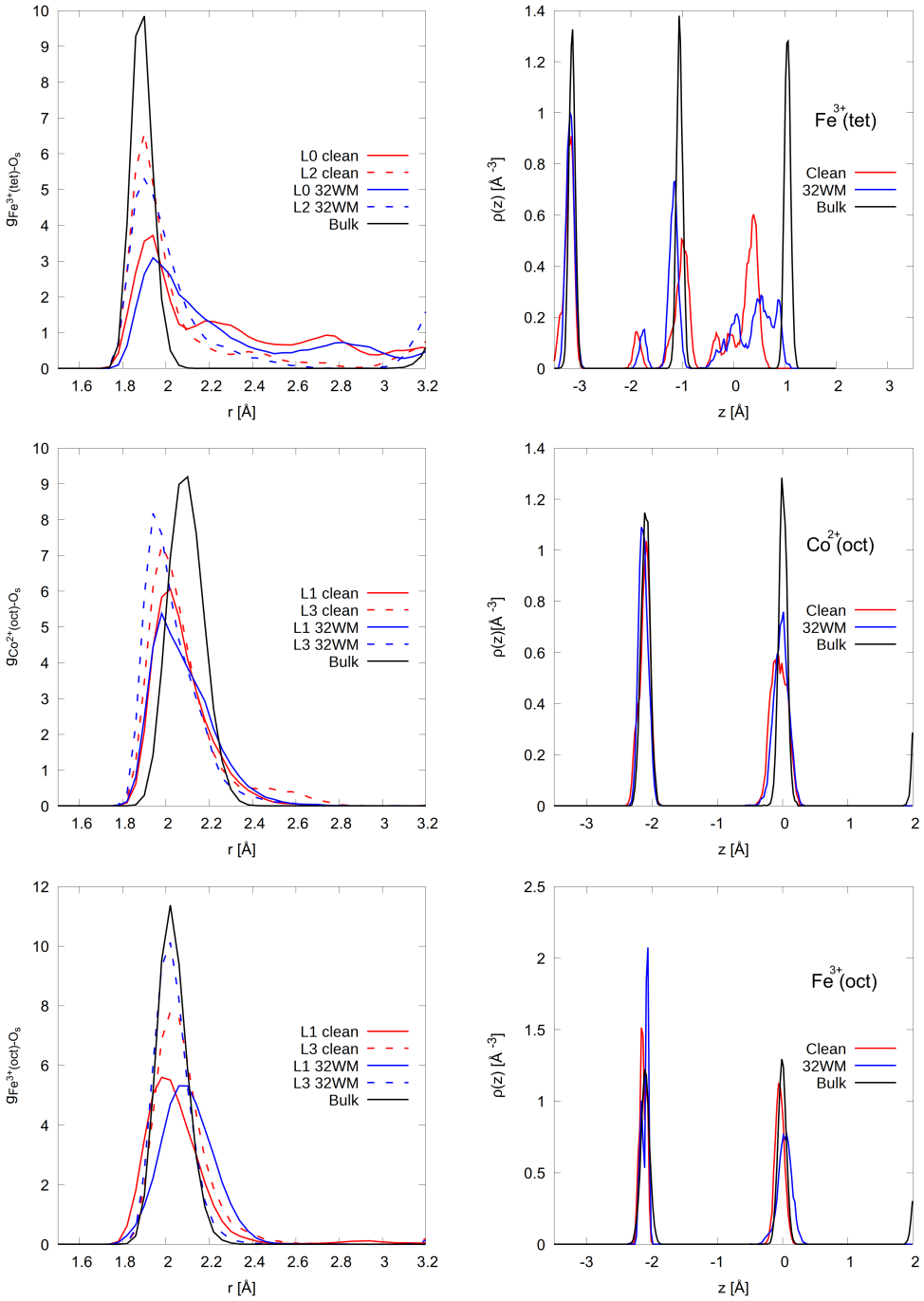

Figure 7. Radial distribution function (**left**) of the lattice oxygens to cobalt and iron ions in the 4 outermost layers (L0-L3) and density profiles (**right**) of the latter on the A-terminated surface. The center of mass of layer L1 (see Figure 1) is taken as reference position z = 0.

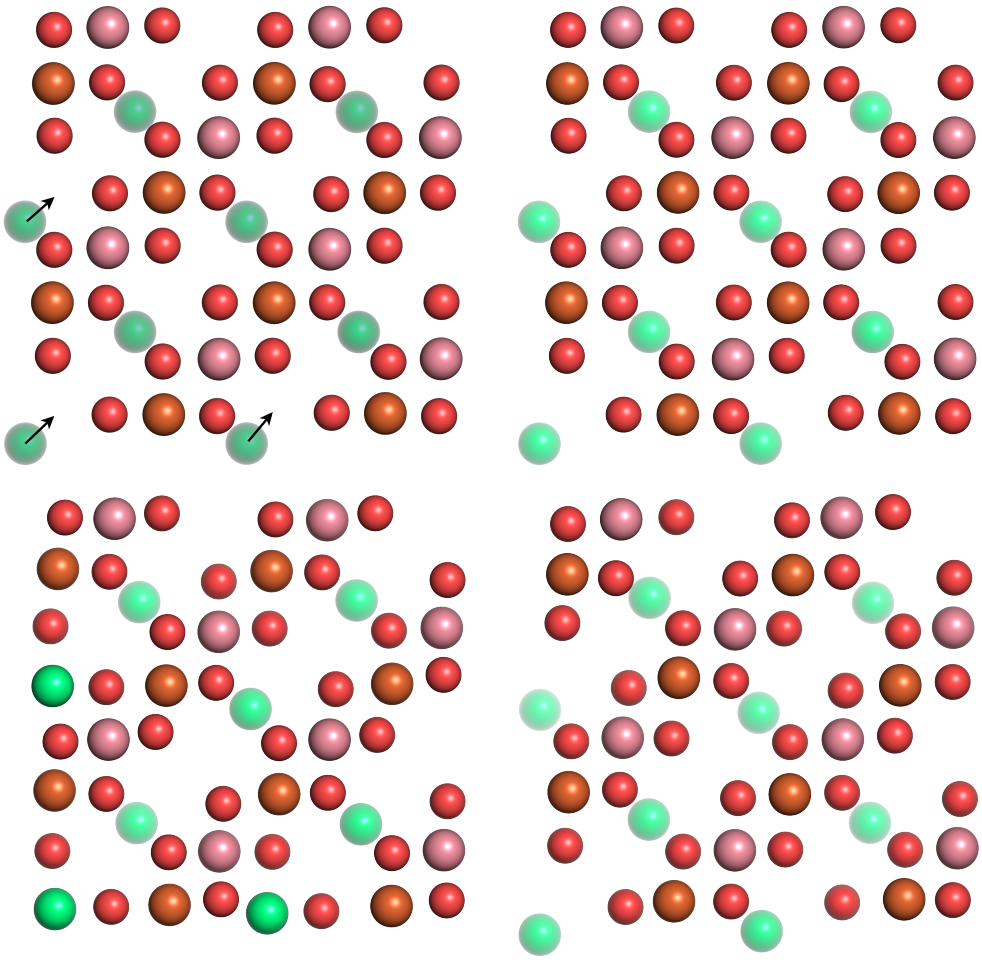

Figure 8. Top views of the initial (top row) and final (after 10 ps; bottom row) surface structures for B-terminated water-free (**left**) and water-covered (**right**) $CoFe_2O_4$(001) surfaces, with atom coloring Fe^{3+}(oct): brown, Fe^{3+}(tet): green, Co^{2+}: purple, O: red as in Figure 2. Fe^{3+}(tet) ions below the top surface layers are partially grayed out. The arrows indicate the reconstruction of the Fe^{3+}(tet).

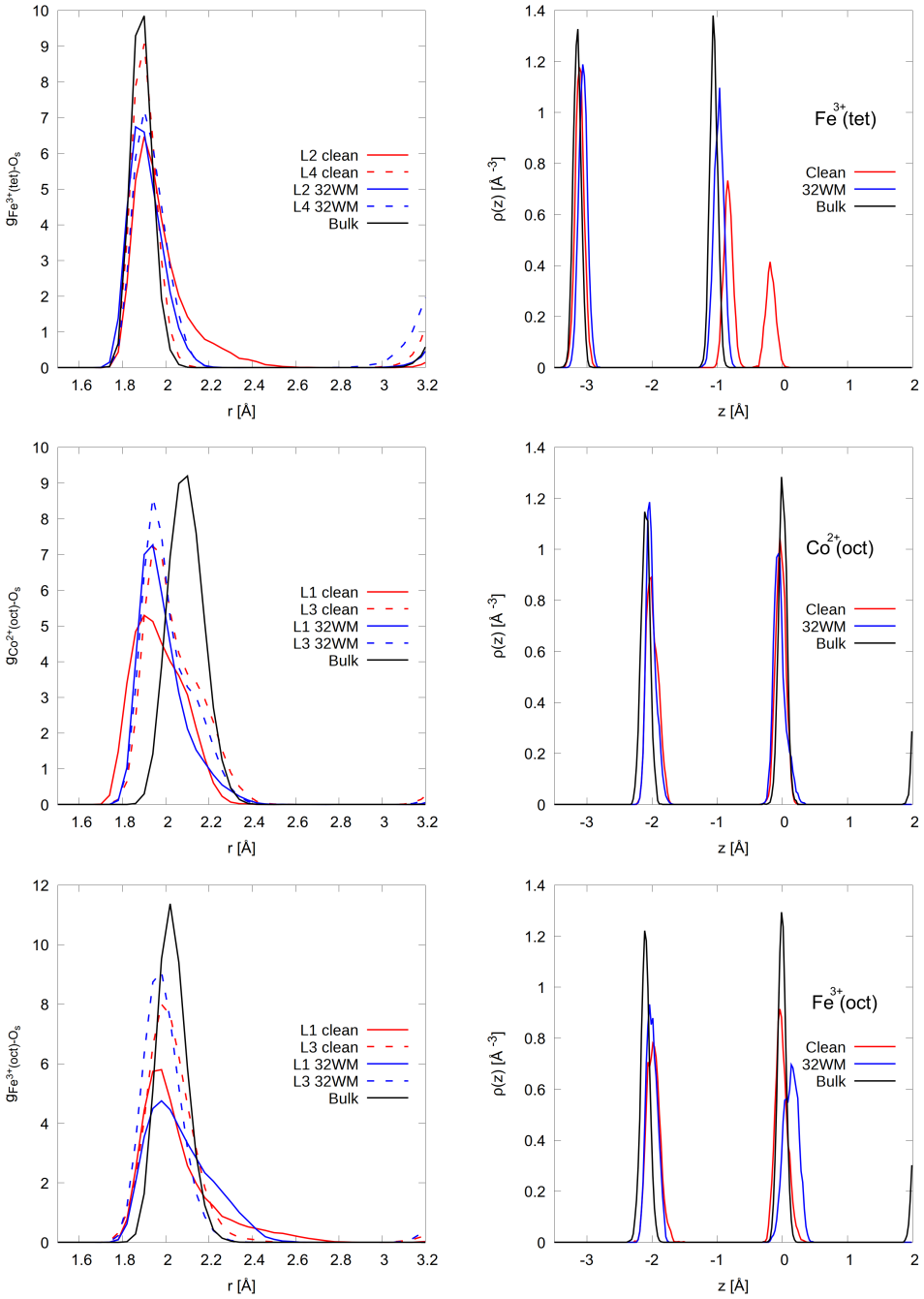

Figure 9. Radial distribution function (**left**) of the lattice oxygens to the cobalt and iron ions in the 4 layers outermost (L1–L4) and density profiles (**right**) of the latter on the B-terminated surface. The center of mass of layer L1 (see Figure 1) is taken as reference position z = 0.

4. Conclusions

Our investigations show that, on both the A- and B-terminations, water is partially dissociated in the contact layer. Molecular water can bind on all cation sites, while hydroxide binds to specific sites. On the A-terminated surface, hydroxide molecules mainly bind on the 2-fold coordinated iron ions Fe^{3+}(tet), while on the B-terminated surface, they sit exclusively on top of the 5-fold coordinated iron ions Fe^{3+}(oct) which are more reactive. The dissociation degree on the A-terminated surface is higher than on the B-termination (A: 7/24, 30% B:3/16, 19%). Following water dissociation, proton transfer to a nearby surface oxygen occurs, resulting in a surface hydroxide. On the A-termination, proton transfers to the surface oxygens O1 in the topmost layer (L1) that is coordinated to one

Fe^{3+}(tet) in the adjacent subsurface layer L2, which is more pronounced, while on the B-termination, it occurs exclusively on the O2 surface oxygens in the layer L1. Both surface terminations undergo reconstruction under dry conditions. The Fe^{3+}(tet) in the topmost layer L0 on the A-termination and those in L2 on the B-termination move towards the nearby unoccupied octahedral voids in layer L1. Water partially lifts the reconstructions on the A-termination and does it completely on the B-termination, as on the latter, the undercoordinated surface atoms converge faster towards their bulk-like environment in the presence of a thin film of 32 water molecules.

Author Contributions: Conceptualization, T.K. and S.K.; methodology, T.K. and S.K.; validation, S.K.; formal analysis, T.K.; investigation, T.K.; resources, T.K., A.H.O. and S.K.; data curation, T.K. and S.K.; writing—original draft preparation, T.K. and S.K.; writing—review and editing, S.K.; visualization, T.K. and A.H.O.; supervision, S.K.; project administration, S.K.; funding acquisition, S.K. All authors have read and agreed to the published version of the manuscript.

Funding: This research was funded by the Deutsche Forschungsgemeinschaft (DFG, German Research Foundation)—388390466—TRR 247.

Institutional Review Board Statement: Not applicable.

Informed Consent Statement: Not applicable.

Data Availability Statement: Not applicable.

Acknowledgments: This study was funded by the Deutsche Forschungsgemeinschaft (DFG, German Research Foundation)—388390466—TRR 247 within the work of Project A6. The authors gratefully acknowledge the computing time granted by the Center for Computational Sciences and Simulation (CCSS) of the Universität of Duisburg-Essen and provided on the supercomputer magnitUDE (DFG grants INST 20876/209-1 FUGG, INST 20876/243-1 FUGG) at the Zentrum für Informations- und Mediendienste (ZIM). A.H.O. is thankful to the International Max Planck Research School for Interface Controlled Materials for Energy Conversion (IMPRS-SurMat) for a Ph.D. Fellowship.

Conflicts of Interest: The authors declare no conflict of interest.

References

1. Zhao, Q.; Yan, Z.; Chen, C.; Chen, J. Spinels: Controlled Preparation, Oxygen Reduction/Evolution Reaction Application, and Beyond. *Chem. Rev.* **2017**, *117*, 10121–10211. [CrossRef] [PubMed]
2. Verwey, E.; Heilmann, E. Physical properties and cation arrangement of oxides with spinel structures I. Cation arrangement in spinels. *J. Chem. Phys.* **1947**, *15*, 174–180. [CrossRef]
3. Guillaud, C. Propriétés magnétiques des ferrites. *J. Phys. Radium* **1951**, *12*, 239–248. [CrossRef]
4. Fritsch, D.; Ederer, C. Epitaxial strain effects in the spinel ferrites $CoFe_2O_4$ and $NiFe_2O_4$ from first principles. *Phys. Rev. B* **2010**, *82*, 104117. [CrossRef]
5. Chakrapani, K.; Bendt, G.; Hajiyani, H.; Schwarzrock, I.; Lunkenbein, T.; Salamon, S.; Landers, J.; Wende, H.; Schlögl, R.; Pentcheva, R.; et al. Role of Composition and Size of Cobalt Ferrite Nanocrystals in the Oxygen Evolution Reaction. *ChemCatChem* **2017**, *9*, 2988–2995. [CrossRef]
6. Chakrapani, K.; Bendt, G.; Hajiyani, H.; Lunkenbein, T.; Greiner, M.T.; Masliuk, L.; Salamon, S.; Landers, J.; Schlögl, R.; Wende, H.; et al. The Role of Composition of Uniform and Highly Dispersed Cobalt Vanadium Iron Spinel Nanocrystals for Oxygen Electrocatalysis. *ACS Catal.* **2018**, *8*, 1259–1267. [CrossRef]
7. Xu, Y.; Özcan, F.; Zielke, P.; Becker, S.; Heimann, M.; Heese, J.; Chakrapani, K.; Behrens, M.; Bredmose Simonsen, S.; Norby, P.; et al. Continuous Hydrothermal Flow Synthesis of $Co_{1-x}Ni_xFe_2O_4$ (x = 0–0.8) Nanoparticles and Their Catalytic Properties for CO Oxidation and Oxygen Evolution Reaction. *Z. Anorg. Allg. Chem.* **2018**, *644*, 1727–1733. [CrossRef]
8. El Arrassi, A.; Liu, Z.; Evers, M.V.; Blanc, N.; Bendt, G.; Saddeler, S.; Tetzlaff, D.; Pohl, D.; Damm, C.; Schulz, S.; et al. Intrinsic activity of oxygen evolution catalysts probed at single $CoFe_2O_4$ nanoparticles. *J. Am. Chem. Soc.* **2019**, *141*, 9197–9201. [CrossRef]
9. Evans, G.; Kozhevnikov, I.V.; Kozhevnikova, E.F.; Claridge, J.B.; Vaidhyanathan, R.; Dickinson, C.; Wood, C.D.; Cooper, A.I.; Rosseinsky, M.J. Particle size–activity relationship for $CoFe_2O_4$ nanoparticleCO oxidation catalysts. *J. Mater. Chem.* **2008**, *18*, 5518–5523. [CrossRef]
10. Mountapmbeme Kouotou, P.; Vieker, H.; Tian, Z.Y.; Tchoua Ngamou, P.H.; El Kasmi, A.; Beyer, A.; Gölzhäuser, A.; Kohse-Höinghaus, K. Structure–activity relation of spinel-type Co–Fe oxides for low-temperature CO oxidation. *Catal. Sci. Technol.* **2014**, *4*, 3359–3367. [CrossRef]

11. Gu, D.; Jia, C.J.; Weidenthaler, C.; Bongard, H.J.; Spliethoff, B.; Schmidt, W.; Schueth, F. Highly ordered mesoporous cobalt-containing oxides: Structure, catalytic properties, and active sites in oxidation of carbon monoxide. *J. Am. Chem. Soc.* **2015**, *137*, 11407–11418. [CrossRef] [PubMed]
12. Thomas, J.; Thomas, N.; Girgsdies, F.; Beherns, M.; Huang, X.; Sudheesh, V.; Sebastian, V. Synthesis of cobalt ferrite nanoparticles by constant pH co-precipitation and their high catalytic activity in CO oxidation. *New J. Chem.* **2017**, *41*, 7356–7363. [CrossRef]
13. Anke, S.; Falk, T.; Bendt, G.; Sinev, I.; Haevecker, M.; Antoni, H.; Zegkinoglou, I.; Jeon, H.; Knop-Gericke, A.; Schlögl, R.; et al. On the reversible deactivation of cobalt ferrite spinel nanoparticles applied in selective 2-propanol oxidation. *J. Catal.* **2020**, *382*, 57–68. [CrossRef]
14. Falk, T.; Budiyanto, E.; Dreyer, M.; Pflieger, C.; Waffel, D.; Büker, J.; Weidenthaler, C.; Ortega, K.F.; Behrens, M.; Tüysüz, H.; et al. Identification of Active Sites in the Catalytic Oxidation of 2-Propanol over $Co_{1+x}Fe_{2-x}O_4$ Spinel Oxides at Solid/Liquid and Solid/Gas Interfaces. *ChemCatChem* **2021**, *13*, 2942–2951. [CrossRef]
15. Kooti, M.; Afshari, M. Magnetic cobalt ferrite nanoparticles as an efficient catalyst for oxidation of alkenes. *Sci. Iran.* **2012**, *19*, 1991–1995. [CrossRef]
16. Dumitru, R.; Papa, F.; Balint, I.; Culita, D.C.; Munteanu, C.; Stanica, N.; Ianculescu, A.; Diamandescu, L.; Carp, O. Mesoporous cobalt ferrite: A rival of platinum catalyst in methane combustion reaction. *Appl. Catal. A Gen.* **2013**, *467*, 178–186. [CrossRef]
17. Simonescu, C.M.; Tătăruş, A.; CuliŢă, D.C.; Stănică, N.; Ionescu, I.A.; Butoi, B.; Banici, A.M. Comparative Study of $CoFe_2O_4$ Nanoparticles and $CoFe_2O_4$-Chitosan Composite for Congo Red and Methyl Orange Removal by Adsorption. *Nanomaterials* **2021**, *11*, 711. [CrossRef]
18. Zheng, H.; Zhan, Q.; Zavaliche, F.; Sherburne, M.; Straub, F.; Cruz, M.P.; Chen, L.Q.; Dahmen, U.; Ramesh, R. Controlling Self-Assembled Perovskite—Spinel Nanostructures. *Nano Lett.* **2006**, *6*, 1401–1407. [CrossRef]
19. Fan, X.; Guan, J.; Cao, X.; Wang, W.; Mou, F. Low-Temperature Synthesis, Magnetic and Microwave Electromagnetic Properties of Substoichiometric Spinel Cobalt Ferrite Octahedra. *Eur. J. Inorg. Chem.* **2010**, *2010*, 419–426. [CrossRef]
20. Kenmoe, S.; Biedermann, P.U. Water adsorbate phases on ZnO and impact of vapor pressure on the equilibrium shape of nanoparticles. *J. Chem. Phys.* **2018**, *148*, 054701. [CrossRef]
21. Hajiyani, H.; Pentcheva, R. Surface Termination and Composition Control of Activity of the $Co_xNi_{1-x}Fe_2O_4(001)$ Surface for Water Oxidation: Insights from DFT+U Calculations. *ACS Catal.* **2018**, *8*, 11773–11782. [CrossRef]
22. Lu, L.T.; Dung, N.T.; Tung, L.D.; Thanh, C.T.; Quy, O.K.; Chuc, N.V.; Maenosono, S.; Thanh, N.T.K. Synthesis of magnetic cobalt ferrite nanoparticles with controlled morphology, monodispersity and composition: The influence of solvent, surfactant, reductant and synthetic conditions. *Nanoscale* **2015**, *7*, 19596–19610. [CrossRef] [PubMed]
23. Eom, Y.; Abbas, M.; Noh, H.; Kim, C. Morphology-controlled synthesis of highly crystalline Fe_3O_4 and $CoFe_2O_4$ nanoparticles using a facile thermal decomposition method. *RSC Adv.* **2016**, *6*, 15861–15867. [CrossRef]
24. Rushiti, A.; Hättig, C.; Wen, B.; Selloni, A. Structure and Reactivity of Pristine and Reduced Spinel $CoFe_2O_4$ (001)/(100) Surfaces. *J. Phys. Chem. C* **2021**, *125*, 9774–9781. [CrossRef]
25. Kenmoe, S.; Biedermann, P.U. Water aggregation and dissociation on the ZnO(100) surface. *Phys. Chem. Chem. Phys.* **2017**, *19*, 1466–1486. [CrossRef] [PubMed]
26. Kox, T.; Spohr, E.; Kenmoe, S. Impact of Solvation on the Structure and Reactivity of the Co_3O_4 (001)/H_2O Interface: Insights From Molecular Dynamics Simulations. *Front. Energy Res.* **2020**, *8*, 312. [CrossRef]
27. Kenmoe, S.; Lisovski, O.; Piskunov, S.; Bocharov, D.; Zhukovskii, Y.F.; Spohr, E. Water Adsorption on Clean and Defective Anatase TiO_2 (001) Nanotube Surfaces: A Surface Science Approach. *J. Phys. Chem. B* **2018**, *122*, 5432–5440. [CrossRef] [PubMed]
28. Kenmoe, S.; Lisovski, O.; Piskunov, S.; Zhukovskii, Y.F.; Spohr, E. Electronic and optical properties of pristine, N- and S-doped water-covered TiO_2 nanotube surfaces. *J. Chem. Phys.* **2019**, *150*, 041714. [CrossRef]
29. CP2K is freely. T.C.d.g. 2016. Available online: http://www.cp2k.org/.
30. Perdew, J.P.; Burke, K.; Ernzerhof, M. Generalized Gradient Approximation Made Simple. *Phys. Rev. Lett.* **1996**, *77*, 3865–3868. [CrossRef] [PubMed]
31. Grimme, S.; Antony, J.; Ehrlich, S.; Krieg, H. A consistent and accurate ab initio parametrization of density functional dispersion correction (DFT-D) for the 94 elements H-Pu. *J. Chem. Phys.* **2010**, *132*, 154104. [CrossRef]
32. Hubbard, J.; Flowers, B.H. Electron correlations in narrow energy bands. *Proc. R. Soc. Lond. Ser. A Math. Phys. Sci.* **1963**, *276*, 238–257. [CrossRef]
33. Zigla, A.A.; Kox, T.; Mevoa, D.; Assaouka, H.T.; Nsangou, I.N.; Daawe, D.M.; Kenmoe, S.; Kouotou, P.M. Magnesium-Modified Co_3O_4 Catalyst with Remarkable Performance for Toluene Low Temperature Deep Oxidation. *Catalysts* **2022**, *12*, 411. [CrossRef]
34. Zerebecki, S.; Salamon, S.; Landers, J.; Yang, Y.; Tong, Y.; Budiyanto, E.; Waffel, D.; Dreyer, M.; Saddeler, S.; Kox, T.; et al. Engineering of Cation Occupancy of $CoFe_2O_4$ Oxidation Catalysts by Nanosecond, Single-Pulse Laser Excitation in Water. *ChemCatChem* **2022**, *14*, e202101785. [CrossRef]
35. Budiyanto, E.; Zerebecki, S.; Weidenthaler, C.; Kox, T.; Kenmoe, S.; Spohr, E.; DeBeer, S.; Rüdiger, O.; Reichenberger, S.; Barcikowski, S.; et al. Impact of Single-Pulse, Low-Intensity Laser Post-Processing on Structure and Activity of Mesostructured Cobalt Oxide for the Oxygen Evolution Reaction. *ACS Appl. Mater. Interfaces* **2021**, *13*, 51962–51973. [CrossRef]
36. Ulman, K.; Poli, E.; Seriani, N.; Piccinin, S.; Gebauer, R. Understanding the electrochemical double layer at the hematite/water interface: A first principles molecular dynamics study. *J. Chem. Phys.* **2019**, *150*, 041707. [CrossRef] [PubMed]